POLYPUBLIE
Polytechnique Montréal

POLYTECHNIQUE MONTRÉAL
UNIVERSITÉ D'INGÉNIERIE

Titre: Title: Orienting Cellulose Nanocrystal Functionalities Tunes the Wettability of Water-Cast Films

Auteurs: Authors: Charles Bruel, Salomé Queffeulou, Pierre Carreau, Jason Robert Tavares, & Marie-Claude Heuzey

Date: 2020

Type: Article de revue / Article

Référence: Citation: Bruel, C., Queffeulou, S., Carreau, P., Tavares, J. R., & Heuzey, M.-C. (2020). Orienting Cellulose Nanocrystal Functionalities Tunes the Wettability of Water-Cast Films. Langmuir, 36(41), 12179-12189. https://doi.org/10.1021/acs.langmuir.0c01799

Document en libre accès dans PolyPublie
Open Access document in PolyPublie

URL de PolyPublie: PolyPublie URL: https://publications.polymtl.ca/46990/

Version: Version finale avant publication / Accepted version
Révisé par les pairs / Refereed

Conditions d'utilisation: Terms of Use: Tous droits réservés / All rights reserved

Document publié chez l'éditeur officiel
Document issued by the official publisher

Titre de la revue: Journal Title: Langmuir (vol. 36, no. 41)

Maison d'édition: Publisher: American Chemical Society (ACS)

URL officiel: Official URL: https://doi.org/10.1021/acs.langmuir.0c01799

Mention légale: Legal notice: This document is the Accepted Manuscript version of a Published Work that appeared in final form in Langmuir, Copyright © 2020 American Chemical Society after peer review and technical editing by the publisher. To access the final edited and published work see https://pubs.acs.org/doi/10.1021/acs.langmuir.0c01799

Ce fichier a été téléchargé à partir de PolyPublie, le dépôt institutionnel de Polytechnique Montréal
This file has been downloaded from PolyPublie, the institutional repository of Polytechnique Montréal

https://publications.polymtl.ca

Orienting cellulose nanocrystal functionalities tunes the wettability of water-cast films

Charles Bruel,* Salomé Queffeulou, Pierre J. Carreau, Jason R. Tavares, and Marie-Claude Heuzey*

Research Center for High Performance Polymer and Composite Systems (CREPEC), Department of Chemical Engineering, Polytechnique Montreal, PO Box 6079, Stn Centre-Ville, Montreal, QC H3C 3A7, Canada.

E-mail: charles.bruel@polymtl.ca; marie-claude.heuzey@polymtl.ca

Phone: +1-514-340-4711 Ext. 5930. Fax: +1-514-340-4159

Abstract

Cellulose nanocrystal (CNC)-based materials display apparently erratic wetting behaviors with contact angle (CA) variations as large as 30° from sample to sample. This work hypothesizes that it is the orientation of CNC amphiphilic functionalities at the interface with air that causes the variability in CA. By exploiting relationships with Hansen solubility parameters theory, a set of surface tension parameters is proposed for both the polar and the non-polar surfaces of cellulose I_β nanocrystals. These coefficients elucidate the wettability of CNC materials by establishing a correlation between the wetting properties of the air/sample interface and its chemical composition in terms of non-polar moieties. Advancing/receding CA experiments suggest that while spin-coating CNC suspensions yields purely polar films, oven-casting them produces amphiphilic surfaces. We proposed a mechanism where the state of dispersion (individual or agglomerated) in which CNCs reach the air/water interface during casting is

the determining factor: while individual nanocrystals find it more stable to orient their non-polar surfaces toward the interface, the aspect ratio of CNC agglomerates favors an orientation of their polar surfaces. This represents the first compelling evidence of CNC orientation at an interface and can be applied to Pickering emulsions, nanocomposites, and to the production of CNC materials with tuned wettability.

Introduction

Cellulose nanocrystals (CNCs) are biosourced rod-like nanoparticles whose high aspect ratio and mechanical properties may find applications in multiphase and interfacial systems such as nanocomposites, Pickering emulsions, and membranes.[1–4] This potential is favored by the amphiphilic nature of cellulose I_β allomorph, whose surfaces display alternating polar and non-polar regions around their circumferences: this means that a simple rotation around their axis may change the nature of the functionalities exposed by these nanocrystals.[2,5] Polar surfaces are hydroxyl rich and usually negatively charged due to the presence of sulfate half-ester groups introduced during the sulfuric acid hydrolysis production step (the most common approach for large-scale production). Non-polar surfaces display C-H bonds and are described as being thinner than their polar counterparts.[6,7]

Investigating the orientation and the adhesion of CNCs at various interfaces is crucial to predict the stabilizing effect they may bring to multiphase systems. As a measure of a material's cohesive interactions, surface tension, γ, is the main predictor for the work of adhesion between a substrate and its environment. Attempts to estimate CNC surface tension were essentially conducted through contact angle measurements,[8–10] but also through gas chromatography[11] and computer simulations.[12] Experimental approaches carried over large quantities of material usually yield surface tensions values that average the behavior of CNCs and cannot distinguish polar from non-polar surfaces. While computer simulations may overcome this problem, their results cannot be verified experimentally and surface tensions tend to be suspiciously high, with up to $155\,\mathrm{mN\,m^{-1}}$ being reported.[12] This is to be

compared with ∼20 to 50 mN m^{-1} for commodity polymers.[13] Overestimation may arise from the hypotheses that must be formulated for the simulations to converge. Mazeau and Rivet[14] had, for instance, to hypothesize that CNC surfaces are flat and ∼10 nm-wide (nearly twice the diameter of a nanocrystal) in order to study their wetting behavior.

Here, we propose an alternate approach that combines modeling, to discriminate between the amphiphilic surfaces of the nanocrystals, with experimental validation. The model, which does not require any computer simulations, relies on two recent empirical investigations: the first determined the Hansen solubility parameters (HSP) of CNC polar and non-polar surfaces;[6] the other established the first correlations between Hansen solubility and surface tension parameters for solids.[15] The method provides estimates for the surface tension parameters of CNC surfaces that rely on empirical evidences only.

Experimental validation requires the production of macroscopic surfaces with a controlled orientation of the nanocrystals. There, our approach relies on the wetting behavior of CNC thin films: the water contact angle was measured to be as low as ∼10° on films prepared from spin-coated suspensions[8] and as high as ∼45° on films prepared by compressing CNC pellets.[9] Oven-cast films have intermediate water contact angle values.[8,9] The influence of the casting protocol, when discussed, is sometimes attributed to differences in surface roughness between the films.[9] This interpretation does not, however, hold up to scrutiny: ranking the films by roughness, spin-coated films are expected to be the smoothest, then oven-cast films, and finally those prepared from the compression of pellets. Based on Wenzel's equation for hydrophilic materials in the homogeneous wetting regime,[6,16] spin-coated films should hence have the highest water contact angle –the opposite is observed. Dankovich and Gray[8] noted that thicker CNC films (obtained through oven-casting) resulted in higher water contact angle values than thinner films (obtained through spin-coating). Their argumentation revolved around the thickness of the films and their potential for swelling.[17] While significant swelling of CNC films has indeed been reported with polar liquids,[17] this does not explain why large variations are also observed with a non-polar liquid such as diiodomethane.

Instead, our interpretation is that the variations observed in contact angles values capture a reorientation of the amphiphilic moieties of CNC particles at the air/sample interface as a function of the casting protocol. A similar argument is formulated to justify the stability provided by CNC particles at the interface of oil/water Pickering emulsions.[7,18,19] There, CNCs are thought to orient their non-polar surfaces toward the oil and their polar surfaces toward water. If such a mechanism is possible in micro-emulsions, it should also occur at the air/water interface of aqueous CNC suspensions and be reflected by the wettability of the films cast from these suspensions. Bertsch et al.[20],[21] indeed demonstrated that a significant CNC adsorption at the air/water interface into a loose monolayer may occur over time for colloidal CNCs. Salt addition is critical for the formation of a dense viscoelastic layer in dilute conditions, but this requirement decreases with CNC concentration: a viscoelastic layer is observed from 25 mM of NaCl at 0.3 wt% of CNCs, and from 20 mM of NaCl at 0.5 wt% of CNCs.[20,21] At higher concentrations (starting in this work from 3 wt%) and upon drying, it is likely that this process will be observed even in the absence of added salt. What is left to determine is which surfaces these nanoparticles adsorb from at the interface. Our hypothesis is thus that the casting protocol has the potential to influence the migration and the orientation of CNC particles at the interface with air. This interface may then be investigated with liquids, whose wetting behaviors reflect the composition of the sample surface down to the molecular-scale.

Hence, this work first produces estimates for the surface tension parameters of CNC amphiphilic surfaces. These coefficients are used to predict how modeled surfaces, with various ratios of non-polar over polar functionalities, would behave upon wetting. The predictions are then compared with experimental results obtained on thin films that were either oven-cast or spin-coated. This yields an estimation of the surface fractions in non-polar moieties on both kinds of films. Using two probe liquids, ethylene glycol (EG) and diiodomethane (DIM), it is possible to validate our approach. These liquids were selected in order to minimize kinetic effects such as swelling (water was found unsuitable to yield high quality contact

angle data on CNC materials). Our approach establishes that CNCs should be considered as amphiphilic particles that can orient their functionalities at air/sample interfaces and that this orientation process can influence macroscale properties such as surface wettability. A speculative mechanism is proposed to describe the influence of the casting protocol on the composition of the interface. It may apply to the production of CNC materials with tuned wetting behaviors. Finally, by providing the first experimentally-validated estimates for the surface tension parameters of CNC polar and non-polar surfaces, this work opens the field to quantitative predictions of CNC behavior in suspensions and multiphase systems such as Pickering emulsions and polymer blends. Note that a nomenclature of the symbols and abbreviations employed throughout this work is provided in Table SI.1.

Experimental Section

Cellulose nanocrystals

Cellulose nanocrystals were provided by Celluforce (Montreal, QC, Canada) as a spray-dried powder. They were produced through the sulfuric acid hydrolysis of a bleached softwood kraft pulp followed by neutralization with sodium hydroxide. Since morphology has been reported to play a major role in the behavior of CNC particles at interfaces,[5] a detailed structural characterization of the particles is performed in supplementary information (SI). It includes transmission electron microscopy (TEM), elemental analysis, Zeta-potential, and X-ray-diffraction (XRD). Fig. 1.a is a TEM image of the rod-like nanocrystals that shows a mix of individual and agglomerated particles. It was obtained by drying a dilute suspension of nanocrystals over a TEM grid. Nanocrystals are ~7-8 nm wide and ~105-120 nm long based on these analyses (see details and protocols in SI). Fig. 1.b are atomic force microscopy (AFM) height images of CNCs that were either spin-coated (left) or oven-cast (right). The micrographs are 2 µm wide and were flattened (by a second-order polynomial) in order to remove their mesoscale roughness: they highlight the parallel alignment of CNC particles at

the air/sample interface.

For graphical purposes, this work considers CNCs to have an octagonally-shaped cross-section as per Kalashnikova et al.[7] (Fig. 1.c). The validity of this hypothesis is discussed in SI and supported by the deconvolution of the XRD spectra and their analysis using Scherrer's equation.[22–24] Neglecting the extremities of the rod, a cellulose I_β nanocrystal exposes up to four different kinds of lateral surfaces, each corresponding to a lattice plane: (010), (110), $(1\bar{1}0)$, and (200).[5] While (200) surfaces primarily display C-H bonds, the three others are rich in hydroxyl groups and have roughly equivalent chemistries.[6,12,25] They will be referred as non-polar and polar surfaces throughout this work and be represented in yellow and blue, respectively. Hence, CNCs display a majority of polar surfaces that are combined with some non-polar ones. This is coherent with their behavior in suspensions where CNCs display a predominantly polar behavior doubled by a non-polar component.[6,26]

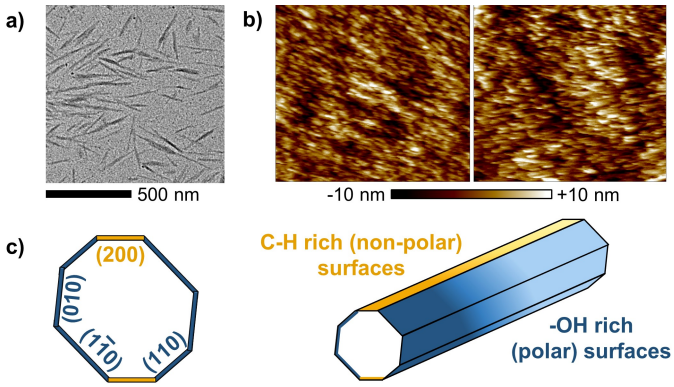

Figure 1: Morphology and representation of cellulose I_β nanocrystals. **(a)** TEM image of individual and agglomerated CNCs. **(b)** AFM height images of spin-coated (left) and oven-cast (right) CNCs. Micrographs are 2 µm wide and were flattened (by a second-order polynomial) in order to remove their mesoscale roughness. **(c)** On the left is the cross-section of a cellulose I_β nanocrystal: polar surfaces –(010), (110), and $(1\bar{1}0)$ lattice planes– are plotted in blue, and non-polar ones –(200) lattice planes– are in yellow. On the right is a scheme of the octogonally-shape nanocrystal: its lateral surfaces are constituted of polar and non-polar stripes.

CNC film preparation

Spray-dried CNCs were dispersed in water at a concentration of 30 mg_{CNC}/mL using an ultrasonic probe (Cole-Parmer), which operated with a CV334 converter and a tapered microtip. The suspensions were prepared adding 15 mL of water atop 0.45 g of CNCs in a glass vial (2.1 cm of radius). As per Beuguel et al.[27], an energy of 4.5 kJ (10 kJ/g_{CNC}) was then provided to the system at a frequency of 20 kHz and a power of ∼30 W using ON-OFF pulses (5 s-2 s) and an ice bath to avoid any overheating. Since our CNCs do not form significant structuring below ∼40 mg_{CNC}/mL,[27] the resulting suspensions are expected to be isotropic. The suspensions were either poured in a polystyrene Petri dish (10 cm of diameter) and placed in an oven (OV-11, MBI Lab Equipment) at 60 °C and near atmospheric pressure (∼0.9 bar) for 24 h, or used for spin-coating. In the latter, a few mL of suspension were placed at the center of a polished n-type Si wafer (15 cm of diameter), that was spun at 500 rpm (revolutions per minute) for 20 s in a spin-coater (Brewer Science CEE-200). Immediately after, the spun-discs were deposited on a hot plate (60 °C) for a few minutes. Drying, evidenced by the apparition of iridescent patterns, occurred within a few seconds. The spin-coating process, from liquid deposition to iridescent patterns formation was typically shorter than 2 min.

While the oven-cast (OC) films were free-standing (thickness of ∼40 µm) and could be analyzed as such, the spin-coated (SC) layer (∼1 µm thick) was stuck on the support. Hence, analyses of SC thin films were carried on the layer still deposited atop the Si wafer. Those requiring a minimal thickness for the sample, such as XRD and elemental analysis, were only performed on the OC films.

Contact angle measurements

Contact angle measurements were performed at room temperature (∼23 °C) on a OCA20 tensiometer (DataPhysics Instruments GmbH) operating with a high-resolution CCD camera and a motorized syringe (0.50 mm of outer diameter). Ethylene glycol (EG) and di-

iodomethane (DIM) were used as probe liquids. Through pendant drop experiments, their surface tensions were found to be within $1\,\mathrm{mN\,m^{-1}}$ ($\sim$2 %) of their theoretical values ($48\,\mathrm{mN\,m^{-1}}$ for EG, and $50.8\,\mathrm{mN\,m^{-1}}$ for DIM). From casting to testing, thin films were stored with covers in a ventilated environment. Prior to analyses, their surfaces were subjected to a cleaning with compressed air in order to desorb any potential contaminant and remove humidity traces. Cleaning was achieved with a compressed air gun operating at $\sim$2 bar for $\sim$1 min.

In a typical static sessile drop experiment, a droplet of 3 µL is grown at the tip of the syringe, far from the sample, at a rate of $0.5\,\mathrm{\mu L\,s^{-1}}$. It is then deposited on the substrate and the measurement is taken after 5 s based on the video footage.

For advancing/receding contact angle (ARCA) experiments, the tip of the needle was first cleaned with the probe liquid, dried, then placed at $\sim$0.5 mm from the substrate. A volume of 4 µL (DIM as probe liquid) or 5 µL (EG) was then injected at a rate of $0.1\,\mathrm{\mu L\,s^{-1}}$. The discrepancy between DIM and EG in terms of injected volumes arises from their differences in terms of dewetting behaviors: a lower receding CA value (as with EG) requires to grow a larger drop in order to witness any receding. Once the injection was completed, and after a delay of at least 5 s (typically $\sim$10 s), the liquid was withdrawn from the substrate at the same rate ($0.1\,\mathrm{\mu L\,s^{-1}}$). The drop remained roughly axissymetric during the whole process.

ARCA measurements were obtained based on video footages. The baseline and the shape of the drop were fitted automatically as a function of the light contrast between the drop, the substrate, and the background. The contact angle was then determined using the Young-Laplace equation. A manual fitting was performed for each test to confirm the validity of the automatically-derived measurements. Measurements were performed during the period where the base diameter of the drop, D^{drop}, was greater than 3 mm (six times the diameter of the needle) in order to minimize the influence of the needle over the shape of the droplet.[28]

A model for the wettability of CNC films based on the orientation of their lattice plane

Contact angles: a background

A liquid droplet sitting on a surface has a three-phase boundary between the liquid, the solid, and the air, that is characterized by its contact angle (CA).[29] Ideal substrates are expected to be flat, rigid, chemically homogeneous, and unperturbed by the chemical interactions they may form with the liquid.[30] There, the Young contact angle, θ_{Y}, is the single CA that may form at rest: it is a thermodynamic equilibrium that may be met independently of the sample's or the drop's history.[29] According to Young's equation, θ_{Y} is a function of the surface tensions of the solid, γ^{s}, of the liquid, γ^{l}, and of the interfacial tension between the liquid and the solid, $\gamma^{\mathrm{s/l}}$:[29]

$$\gamma^{\mathrm{s}} = \gamma^{\mathrm{s/l}} + \gamma^{\mathrm{l}} cos\left(\theta_{\mathrm{Y}}\right) \tag{1}$$

On real substrates, deviations from ideality create hysteresis, defined as a difference between the wetting and dewetting behaviors. Irregularities impede the progression of the liquid upon wetting, and prevent its receding upon dewetting.[29] In a dynamic experiment, the highest CA value is thus measured in advancing conditions: the advancing contact angle, θ_{a}; and the lowest CA in receding conditions: the receding contact angle, θ_{r}. The contact angle hysteresis, H, is defined as $H{=}\theta_{\mathrm{a}}\text{-}\theta_{\mathrm{r}}$ ($H \geq 0°$). H is a direct measure of a sample's deviation from ideality.[29]

There are two kinds of hysteresis: kinetic and thermodynamic.[29–31] Kinetic hysteresis arises from physical and chemical interactions occurring at the interfaces.[30] It includes: swelling, chemical reactions, and reorientation of the functional groups at the liquid/solid interface; evaporation at the air/liquid interface; adsorption of contaminants or vapor molecules at the air/solid interface; or the diffusion of liquid throughout the sample. Thermodynamic

hysteresis is caused by surface heterogeneities in terms of roughness or chemistry.[30] In practice, near ideal substrates have an hysteresis in the range of 1-2°, and H commonly reaches ∼10° for real substrates.[29–31] It may be as high as 50-60° in some circumstances.[32]

In this work, kinetic and roughness-induced hystereses were minimized, respectively by appropriately identifying the most suited probe liquids (SI: section "Minimization of kinetic hysteresis") and by producing films whose surface roughness is in the range of a single nanocrystal diameter (SI: section "Thermodynamic hysteresis"). This leaves chemical heterogeneity as the main source of hysteresis.

Wettability of real chemically heterogeneous surfaces

Assuming an expression for the interfacial tension between the liquid and the solid, $\gamma^{s/l}$, it is possible to measure the theoretical Young contact angle from γ^s and γ^l, only. Several models were proposed for $\gamma^{s/l}$, the most employed being the Owens-Wendt-Rabel-Kaelble (OWRK) model. It splits the total surface tension, γ, into a dispersive, γ_D, and a polar component, γ_P (Eq. 2). γ_P accounts both for dipole-dipole and Lewis acid/base (including H-bonding) interactions.

$$\gamma = \gamma_D + \gamma_P \tag{2}$$

The OWRK model expresses the total interfacial tension $\gamma^{s/l}$ as a geometric mean that considers γ^s and γ^l components:

$$\begin{aligned} \gamma^{s/l} &= \gamma_D^{s/l} + \gamma_P^{s/l} \\ &= \left(\sqrt{\gamma_D^s} - \sqrt{\gamma_D^l}\right)^2 + \left(\sqrt{\gamma_P^s} - \sqrt{\gamma_P^l}\right)^2 \\ &= \gamma^s + \gamma^l - 2\left(\sqrt{\gamma_D^s \gamma_D^l} + \sqrt{\gamma_P^s \gamma_P^l}\right) \end{aligned} \tag{3}$$

Note that a good compatibility between the materials results in a low interfacial tension. It is null ($\gamma^{s/l}$=0) if the components of the liquid match those of the solid. Combining

Eqs. 1&3 yields:

$$cos\left(\theta_{\mathrm{Y}}\right)=\frac{2}{\gamma^{\mathrm{l}}}\left(\sqrt{\gamma_{\mathrm{D}}^{\mathrm{s}}\gamma_{\mathrm{D}}^{\mathrm{l}}}+\sqrt{\gamma_{\mathrm{P}}^{\mathrm{s}}\gamma_{\mathrm{P}}^{\mathrm{l}}}\right)-1 \tag{4}$$

This equation is only valid if $\gamma^{\mathrm{s}}<\gamma^{\mathrm{l}}+\gamma^{\mathrm{s/l}}$, which, in practice, remains the case as long as the surface tension of the liquid is high enough. Otherwise, the liquid totally wets the surface, thus forming a zero-contact angle. Van Oss et al.[33] proposed a threshold of $\gamma^{\mathrm{l}}\gtrapprox 44\,\mathrm{mN\,m^{-1}}$ above which probe liquids should be suitable for the analysis of most common surfaces.

Surface roughness may shift the value of θ_{Y}, and an apparent Young's ("Wenzel") contact angle, θ_{W}, is measured instead.[16,29] In the homogeneous wetting regime, this may be accounted for by the Wenzel equation, in which r_{surf}, dimensionless, is defined as the surface area of the sample divided by its projected surface area (r_{surf}=1 for a perfectly smooth surface):

$$cos\left(\theta_{\mathrm{W}}\right)=r_{\mathrm{surf}}cos\left(\theta_{\mathrm{Y}}\right) \tag{5}$$

r_{surf} stood at $1<r_{\mathrm{surf}}\leq 1.02$ for all our samples due to their relative flatness (see SI). Our modeling hence assumes that $cos\left(\theta_{\mathrm{W}}\right)\approx cos\left(\theta_{\mathrm{Y}}\right)$.

Chemical heterogeneity may be accounted for using a generalized Cassie-Baxter equation.[34] CNCs are amphiphilic particles, on which the liquid is expected to form a Young's contact angle equal to $\theta_{\mathrm{Y}}^{\mathrm{ps}}$ with polar surfaces ("ps") that have a higher surface energy, and equal to $\theta_{\mathrm{Y}}^{\mathrm{nps}}$ with non-polar surfaces ("nps") that have a lower surface energy ($\theta_{\mathrm{Y}}^{\mathrm{nps}}>\theta_{\mathrm{Y}}^{\mathrm{ps}}$). On a substrate composed by a mix of these polar and non-polar surfaces, with respective surface fractions of f^{ps} and f^{nps} (with f^{ps}=1-f^{nps}), a composite contact angle, θ_{comp}, is measured:[34]

$$cos\left(\theta_{\mathrm{comp}}\right)=f^{\mathrm{nps}}cos\left(\theta_{\mathrm{Y}}^{\mathrm{nps}}\right)+\left(1-f^{\mathrm{nps}}\right)cos\left(\theta_{\mathrm{Y}}^{\mathrm{ps}}\right) \tag{6}$$

Combining Eq. 6 with Eq. 4 applied to polar and non-polar surfaces yields:

$$cos\left(\theta_{\mathrm{comp}}\right) = \frac{2}{\gamma^{\mathrm{l}}}\left[f^{\mathrm{nps}}\left(\sqrt{\gamma_{\mathrm{D}}^{\mathrm{nps}}\gamma_{\mathrm{D}}^{\mathrm{l}}} + \sqrt{\gamma_{\mathrm{P}}^{\mathrm{nps}}\gamma_{\mathrm{P}}^{\mathrm{l}}}\right) + \left(1 - f^{\mathrm{nps}}\right)\left(\sqrt{\gamma_{\mathrm{D}}^{\mathrm{ps}}\gamma_{\mathrm{D}}^{\mathrm{l}}} + \sqrt{\gamma_{\mathrm{P}}^{\mathrm{ps}}\gamma_{\mathrm{P}}^{\mathrm{l}}}\right)\right] - 1 \quad (7)$$

CNC surface tension parameters

Eq. 7 relates the predicted contact angle formed by the liquid over the sample, θ_{comp}, to its composition, f^{nps}. It assumes that the surface tension components of the solid ($\gamma_{\mathrm{D}}^{\mathrm{nps}}$, $\gamma_{\mathrm{P}}^{\mathrm{nps}}$, $\gamma_{\mathrm{D}}^{\mathrm{ps}}$, and $\gamma_{\mathrm{P}}^{\mathrm{ps}}$) can be estimated. This was achieved by exploiting the empirical correlations between surface tension and Hansen solubility parameters (HSP). The HSP of CNCs were determined in a previous work.[6] HSP represent a set of three parameters: δ_{D}, δ_{P}, and δ_{H}, which account for the potential of the surface in terms of dispersive, polar (dipole-dipole), and hydrogen-bonding (and other Lewis acid/base) interactions, respectively.[35] They are expressed as the square-root of an energy density (in $\mathrm{MPa}^{1/2}$). The polar surfaces of CNCs had estimated HSP of $\{\delta_{\mathrm{D}}^{\mathrm{ps}}; \delta_{\mathrm{P}}^{\mathrm{ps}}; \delta_{\mathrm{H}}^{\mathrm{ps}}\} = \{18.1;\ 20.4;\ 15.3\} \pm \{0.5;\ 0.5;\ 0.4\}\ \mathrm{MPa}^{1/2}$, while the non-polar surfaces were estimated at: $\{\delta_{\mathrm{D}}^{\mathrm{nps}}; \delta_{\mathrm{P}}^{\mathrm{nps}}; \delta_{\mathrm{H}}^{\mathrm{nps}}\} = \{17.4;\ 4.8;\ 6.5\} \pm \{0.3;\ 0.5;\ 0.6\}\ \mathrm{MPa}^{1/2}$.[6] Together, they constitute the total (or "Hildebrand") solubility parameter, δ_{T} (Eq. 8), that accounts for the potential of cohesion between a substrate and its environment.

$$\delta_{\mathrm{T}} = \left(\delta_{\mathrm{D}}^2 + \delta_{\mathrm{P}}^2 + \delta_{\mathrm{H}}^2\right)^{1/2} \quad (8)$$

HSP are by definition closely related to surface tension since they both relate to the amount of interactions that a material may form with its environment. Hence, it should be possible to express the surface tension as a function of HSP. While previous models also relied on molar volume,[36–39] Jia and Shi[40] recently proposed a direct correlation between γ_{D} and δ_{D} that was applicable to liquids and polymers. Yu and Hou[15] generalized these models to the various components of surface tension. Four empirical equations were proposed, γ=f(δ_{T}) (Eq. 9); γ=f(δ_{D}, δ_{P}, δ_{H}) (Eq. 10); γ_{D}=f(δ_{D}) (Eq. 11); and γ_{P}=f(δ_{P}, δ_{H}) (Eq. 12). Two further

correlations explored in their work, γ_P=f(δ_P) and γ_P=f(δ_H), are not considered here: these correlations have systematic deviations at high γ_P values (over- or underestimatations). It is consistent with the fact that γ_P accounts for all non-dispersive interactions, i.e for polar and Lewis acid/base interactions. It should thus be predicted from both δ_P and δ_H as in Eq. 12.

$$\gamma = 1.88\delta_T^{0.94} \tag{9}$$

$$\gamma = 0.12\left[\delta_D + 0.25\left(\delta_P + \delta_H\right)\right]^{1.86} \tag{10}$$

$$\gamma_D = 0.035\delta_D^{2.34} \tag{11}$$

$$\gamma_P = 4.30 \times 10^{-2}\left(\delta_P + \delta_H\right)^{1.75} \tag{12}$$

Eq. 9 gives estimates that are slightly smaller than those provided by Eq. 10. Considered together, they provide a lower and an upper bound for CNC surface tensions with γ^{ps} and γ^{nps} ranging from ∼47.8 to 55.2 mN m^{-1} and from ∼30.3 to 32.2 mN m^{-1}, respectively. Through Eqs. 11&12, it is possible to estimate the dispersive and polar components and check that their sum fall within these ranges. Uncertainties reported here are those that arise from HSP. For the polar surfaces, the sum of γ_D^{ps} (30.7±2.0 mN m^{-1}) and γ_P^{ps} (22.4±1.0 mN m^{-1}) yields a γ^{ps} of 53.1±3.0 mN m^{-1}. For the non-polar surfaces, it was γ_D^{nps}=28.0±1.1 mN m^{-1} and γ_P^{nps}=3.0±0.5 mN m^{-1} for a sum of γ^{nps}=31.0±1.6 mN m^{-1}. These surface tension values, summarized in Table 1, fall within the ranges calculated through Eqs. 11&12 and are considered in the rest of this work.

Despite being more conservative than those published previously (Table SI.4), these estimates are in line with what can be expected from a polymeric material (∼20 mN m^{-1} to 50 mN m^{-1} for commodity polymers[13]). Historically, characterizing surface tension has been

challenging for cellulose rich materials.[8] Wood, itself, is commonly measured in a range as large as ∼40 to 90 mN m^{-1}.[41] Besides variations in the samples' composition, issues in contact angle measurements arise from the potential porosity, swelling behaviors, and anisotropic roughness of the material. These are all susceptible to lower the contact angle values measured at the interface between the sample and the liquid, which leads to an overestimation of the solid apparent surface tension. Since previous CA studies all relied on water as a probe liquid and that water interacts strongly with CNCs,[6,17,42] our interpretation is that these works[8,9] overestimated the surface tension of CNCs.

Table 1: Surface and interfacial tension parameters (expressed in mN m^{-1}). Our approach distinguishes between polar and non-polar surfaces for the parameters of cellulose I_β nanocrystals (see Fig. 1). References for the surface tension of liquids are provided in SI. "Abbr." stands for the abbreviation through which the substrates are referred to within the text.

		Surface tension parameters			**Interfacial tensions**[a,b]		
Substrate	Abbr.	γ	γ_D	γ_P	ps	nps	w
Polar surfaces	ps	53.1±3.0[c]	30.7±2.0[c]	22.4±1.0[c]	0	-	-
Non-polar surfaces	nps	31.0±1.6[c]	28.0±1.1[c]	3.0±0.5[c]	∼9.0	0	-
Water	w	72.8	21.8	51.0	∼6.4	∼29.6	0
Hexadecane	h	27.0	∼27.0	∼0.0	∼22.5	∼3.0	∼51.3
Ethylene glycol	EG	48.0	22.6	25.4	∼0.6	∼11.2	-
Diiodomethane	DIM	50.8	48.5	2.3	∼12.3	∼2.8	-

[a] The interfacial tension with air is assumed to be equal to the surface tension γ.
[b] Estimated based on the Owens-Wendt-Rabel-Kaelble (OWRK) model (Eq. 3).
[c] $\gamma=\gamma_D+\gamma_P$, with γ_D and γ_P calculated from Eqs. 11&12, respectively. Uncertainties reflect those on the HSP values.

Results and discussion

Wettability results

The various phases of an ARCA experiments and the process through which they were analyzed are presented in SI (section "ARCA experiments and analyses"). The protocol was established in order for surface tension to dominate the force balance at all times.

The ratio between the hydrodynamic forces and the surface tension of the liquid, γ^l, is defined as the capillary number, N_{Ca} (Eq. SI.4). The ratio between the gravitational forces and γ^l is defined as the Bond number, N_{Bo} (Eq. SI.5). In our experiments, the surface tension largely dominated the force balance by 2 to 3 orders of magnitude (see SI, section "Capillary and Bond numbers"). In terms of importance, it is followed by gravitational forces ($N_{Bo} \approx 10^{-2}$-10^{-3}) and then viscous forces ($N_{Ca} \approx 10^{-5}$-10^{-6}). ARCA results may hence be modeled based on surface tension-related considerations only. Furthermore and according to Strobel and Lyons[31], $N_{Ca}<10^{-5}$ generally ensures that the CA measured at the moving three-phase boundary is equal to that measured just after it stops, i.e. that it corresponds to a thermodynamic state. Overall, this condition was verified during our experiments.

To account for the local nature of a drop-based measurement (analysis of few mm^2 only), each film was analyzed on at least three locations and at least three films were produced for each condition. It represents a minimum of 9 repetitions per experimental condition (excepted θ_r^{EG}, which is based on 3 repetitions only). Uncertainties reported in the text and error bars plotted on the graphs are standard deviations. A full breakdown of the results and their statistical analysis, including 95% confidence intervals, is provided in Table SI.5.

Figs. 2.a&c plot the wettability results obtained with DIM (in purple) and EG (in green) on spin-coated and oven-cast films, respectively. ARCA measurements on OC films yielded θ_a (empty triangles up) and θ_r (empty triangles down) values of 41.0±4.3° and 15.0±1.8° with EG. It was 46.1±1.2° and 16.7±1.3° with DIM. These imply significant hysteresis, H, of ∼26° and ∼30°, respectively.

On the SC films, contact angles values dropped to θ_a=10.2±0.6° and θ_r=0° (no receding) with EG. The lack of any receding prevents an accurate determination of the hysteresis, which may only be said to be smaller than ∼10°. Note that no significant variations were observed by increasing the drying time of the spin-coated films from a few minutes to 24 h (same conditions as the oven-cast films). With DIM, θ_a and θ_r were measured at 34.8±3.4° and 11.6±1.8°, corresponding to an hysteresis of ∼23°. It was a concern that the spin-coated

layer could be too thin to prevent the substrate from affecting the measurement, especially for EG, which seems to swell the film (θ_r=0°). However, preliminary tests performed on bare Si wafers yielded EG advancing contact angles that were greater than those measured on the spin-coated films (14.1±0.5° instead of 10.2±0.6°). Furthermore, CA measurements performed on films spun at 4000 rpm (and thus thinner than those prepared at 500 rpm) yielded results that were not statistically different (11.2±0.5° instead of 10.2±0.6°). Hence, we do not believe the substrate to influence the measurements: the abrupt lowering in CA values observed with EG between oven-cast and spin-coated films may be attributed to a variation at the surface of the CNC coating rather than to an influence of the thickness or of the substrate.

Since kinetic hysteresis and surface roughness were preemptively minimized, the concordant variation in CA hysteresis between the samples for both EG and DIM can be attributed to the surface chemistry of the films: spin-coated films are chemically more homogeneous than oven-cast ones. The fact that this decrease in H is driven by a drop of the advancing contact angle values suggests that spin-coated films have a higher apparent surface energy. Thus, spin-coating a CNC suspension, instead of oven-casting it, leads to an impoverishment of air/sample interfaces in non-polar moieties. Furthermore, the lack of any receding with EG points to a very good interface between the SC film and the probe liquid. Since EG has interfacial tensions (Eq. 3) of $\sim$0.6 mN m^{-1} and $\sim$11.2 mN m^{-1} with the polar and non-polar surfaces of CNCs, respectively, this lack of receding is coherent with the surface being rich in polar moeities.

Chemical composition of air/sample interfaces

The most likely interpretation from wettability results is that oven-cast films are richer in (200) surfaces than spin-coated substrates, which translates into a greater chemical homogeneity for the latter. This interpretation may be confronted with the projections derived from Eq. 7 by plotting θ_{comp} as a function of the surface fraction in non-polar surfaces, f^{nps}

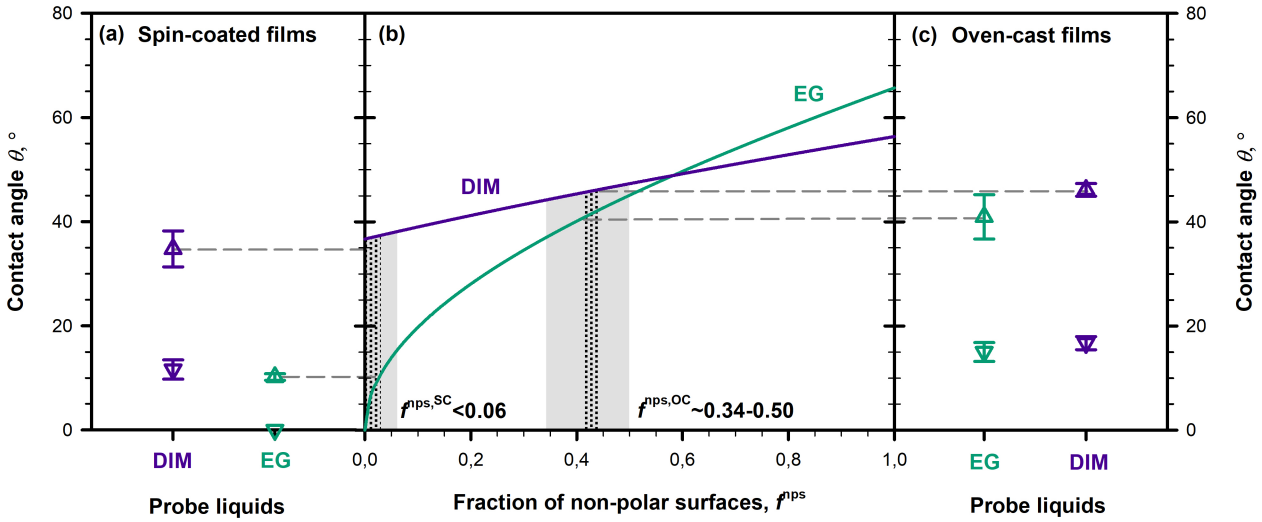

Figure 2: ARCA results for spin-coated **(a)** and oven-cast **(c)** films and their predictions in terms of non-polar fraction, f^{nps}, for the air/sample interface **(b)**. EG and DIM results are plotted in green and purple, respectively. Average θ_{a} values are represented by empty triangles up and θ_{r} values by empty triangles down. In **(b)**, filled lines are the plots of θ_{a} as a function of f^{nps} (Eq. 7) for EG and DIM. The projection of θ_{a} values (grey dashed lines) over these plots provides estimates for the samples' surface content in non polar surfaces. The consistency observed between the f^{nps} predictions derived from EG and DIM (with $\sim$0.02-0.03 between both predictions, highlighted by the dotted areas) confirms the validity of CNC surface tension parameters. Error bars in **(a)**&**c** are standard deviations. Their influence on the determination of f^{nps} is highlighted by the grey areas in **(b)**.

(Fig. 2.b). Considering the smoothness of CNC thin films and their propensity for kinetic phenomena such as swelling, the advancing contact angle is likely to be the most representative estimate of the composite contact angle θ_{comp} in the generalized Cassie-Baxter equation (Eq. 7). Furthermore, advancing contact angles are the most representative CA to detect non-polar moieties.[31,43] This is because low surface tension areas tend to prevent the liquid from advancing, which reflects on θ_{a} values.

Projecting the advancing contact angle values on our model (hypothesis $\theta_{\mathrm{a}} \approx \theta_{\mathrm{comp}}$) returns an estimate of f^{nps}. This projection is highlighted on Fig. 2 by the dashed lines that cross from Fig. 2.a to 2.b, and from 2.c to 2.b, respectively. f^{nps} estimates, whether determined from EG or DIM advancing contact angle values, are consistent: they are in

the range of ∼0.42-0.44 and ∼0-0.03 for oven-cast and spin-coated films, respectively. These ranges may be extended to ∼0.34-0.50 and ∼0-0.06 once the standard deviations on θ_a values are considered. It is consistent with our previous findings: spin-coated films are poorer in non-polar surfaces and chemically more homogeneous than oven-cast substrates.

An analysis of the standard deviations highlights that reproducibility is better through spin-coating than through oven-casting. The large uncertainty observed on f^{nps} (0.34 to 0.50) for oven-cast films actually arises from film-to-film variations. This is highlighted in Fig 3.a, where EG advancing contact angle values measured for each film are plotted as a function of the model predictions for f^{nps}. EG was chosen for its greater sensitivity to the orientation of CNCs. Average θ_a values for spin-coated and oven-cast films are represented by green triangles (as in Fig. 2). θ_a values for each film are plotted in black (SC films) or brown (OC films). The figure's inset is a zoom to help the visualization of the spin-coated results. There are little deviations from sample to sample and spin-coating seems to repeatably yield thin films whose f^{nps} are in the range of 0.02-0.03 (based on EG results). For oven-cast films, uncertainties on f^{nps} are within ±0.03, which suggests that surface heterogeneities are well dispersed across the sample. However, each film is statistically different from the other.

To investigate further the reproducibility of the oven-casting process, 7 new OC films were prepared and investigated through static sessile drop measurements. In our case, static sessile drop measurements fell within ∼1° of the advancing contact angle values, meaning that they constitute an effective way to quickly probe a larger amount of samples. Fig 3.b plot the distribution of 30 sessile drop CA and confirms the low repeatibility of the oven-casting process: CA values spread over nearly 40°, from ∼12° to ∼50°. CA measurements at the bottom of the distribution (pointed by the red arrow) were measured on different locations of a same film that apparently failed to orient its non-polar fonctionnalities toward the air/sample interface. Hence, over the 10 oven-cast films we analyzed (3 through ARCA and 7 through sessile drop measurements), 9 managed to orient at different extents their non-polar functionalities to the air interface and produced EG contact angles ranging from ∼30

to ∼50°. The last film produced CA values ranging from ∼12 to ∼16°, which is close to what can be measured on spin-coated films (θ_a=10.2±0.6°). Sessile drop measurements performed on the same films with DIM (Fig 3.c) show a lesser variability from film to film, which underlines the greater sensitivity of EG to non-polar surface orientation. The red arrow in Fig 3.c points towards the results that were gathered from the film already highlighted in Fig 3.b.

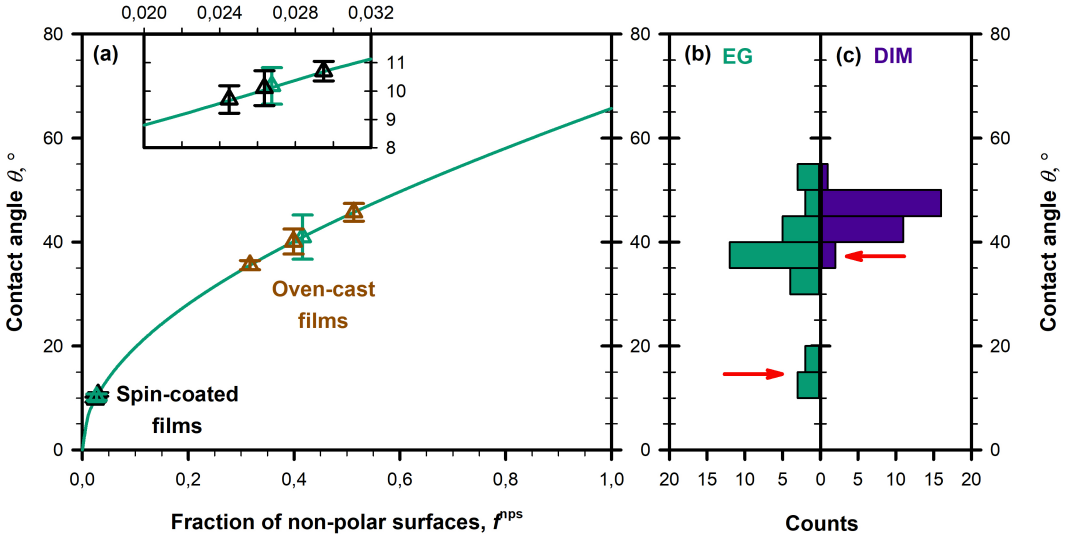

Figure 3: Repeatably of CNC orientation during the spin-coating and oven-casting processes based on EG results **(a)**. The green line and the green triangles up are the plots for Eq. 7 and for the average advancing CA values (see Fig. 2). The black and brown triangles up represent the advancing CA values measured for each of the spin-coated and oven-cast films, respectively. The insert is a zoom of the spin-coated results for greater readability. Error bars are standard deviations. Sessile drop measurements taken on 7 additional oven-cast films with EG **(b)** and DIM **(c)**. The results pointed by the red arrows are from a single data set, taken on a film that apparently failed to orient its non-polar functionalities at the air/sample interface to the same extent as the 6 other samples.

Speculative mechanism for CNC orientation at the air/water interface

Based on Eq. 3, water has interfacial tensions of $\gamma^{ps/w}$=6.4 mN m^{-1} and $\gamma^{nps/w}$=29.6 mN m^{-1} with the polar and non-polar surfaces of CNCs, respectively (Table 1). To understand what may happen in suspensions, it is possible to calculate the energy variations that result from the various options available to the nanocrystal. Fig. 4 plots these various paths, which involve migration to the air/water interface and/or agglomeration, and speculates a mechanism for CNC orientation at the air/sample interface. In the case of interfacial migration, a scenario in which the nanocrystal remains fully immersed in water (with the exception of the adsorbed surfaced) was considered: the influence of CNC vertical positioning at the air/water interface over the energy variation was found to be secondary and was hence neglected. The exact normal positioning of CNCs at interfaces remains to be computed: experimentally, the nanocrystals were reported to be mostly immersed in water at air/water interfaces[20,21] and fully immersed in water at oil/water interfaces.[19] Calculations were done by amalgamating surface tensions with surface energies, which equates to neglecting the heat generated by the process.[29] This also neglects the energy variations caused by ionic bond dissociation (occurring on the sulfate half-ester groups of CNCs). While CNC negative charges may have an effect on the kinetics of the processes described here-below (because of electrostatic stabilization for instance), energy variations associated with these charges are small in front of interfacial phenomena and should not affect the orientation taken by CNC particles at the air/water interface (justification provided in SI). It is worth underlining that beyond energy calculations, the mechanism hypothesized in this section yet remains to be supported by experimental evidences; parts of its limitations involve the true extent to which the influence of surface charges remains secondary when compared to interfacial tension variations.

When an individual CNC (Fig. 4.a) migrates from the water bulk towards the air/water interface, it removes an air/water and a water/solid interface and creates an air/solid one.

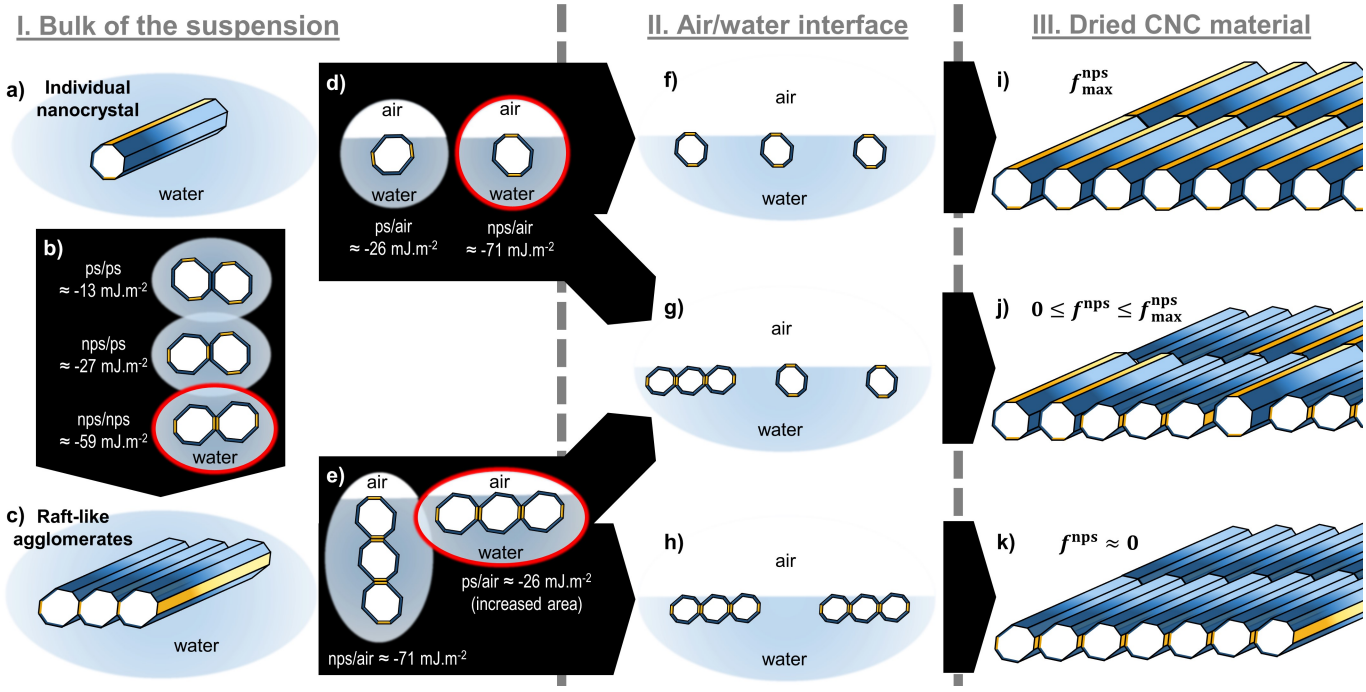

Figure 4: Speculative mechanism for CNC orientation at the air/sample interface. Assuming CNCs are initially well dispersed **(a)**, they may either migrate to the air/water interface as individual nanocrystals or first agglomerate in the water bulk. Upon agglomeration **(b)**, CNCs preferentially assemble their non-polar surfaces to form raft-like structures **(c)**. Upon migration towards the air/water interface, individual CNCs orient their non-polar surfaces towards the air **(d)**. 2-D agglomerates may, however, prefer to orient their polar surfaces if their cross-sectional aspect ratio is large enough **(e)**. Depending on the state of CNC dispersion within the water bulk, the air/water interface may be populated by individual nanocrystals only **(f)**, by a mix of individual and agglomerated particles **(g)**, or by agglomerated CNCs only **(h)**. Upon casting, these result into thin films whose surface is either amphiphilic **(i)&(j)** or purely polar **(k)**. The fraction of non-polar surfaces that a film can expose should reach a maximum of $f_{\max}^{\mathrm{nps}}$ in **(i)**, whose amplitude is a function of the nanocrystals' geometry, and a minimum of ~0 in **(k)**.

The surface energy difference may thus be calculated as $\Delta E \approx \gamma^{\mathrm{nps}}\text{-}\gamma^{\mathrm{nps/w}}\text{-}\gamma^{\mathrm{w}} \approx \text{-}71\,\mathrm{mJ\,m^{-2}}$ if a non-polar surface adsorbs at the air/water interface, and as $\Delta E \approx \text{-}26\,\mathrm{mJ\,m^{-2}}$ if it is a polar surface. Therefore, the air/water interface is better stabilized by the adsorbtion of a non-polar surface (Fig. 4.d). This assumes that the surface areas in terms of polar and non-polar moieties are comparable, which is roughly the case for the sidewalls of an individual nanocrystal.

Instead of migrating towards the air/water interface, CNCs could agglomerate (Fig. 4.b):

matching two polar surfaces together yields an energy variation of ∼-13 mJ m^{-2}, it decreases to ∼-27 mJ m^{-2} for a polar surface agglomerated with a non polar one, and to ∼-59 mJ m^{-2} for two non-polar surfaces together. In aqueous suspensions, CNCs hence find it more favorable to agglomerate by matching their non-polar surfaces together. Repeating the process yields raft-like structures assembled by their (200) surfaces (Fig. 4.c). Similar 2-D aggregates were reported by Uhlig et al.[44] for aqueous suspensions of sulfuric acid-hydrolyzed CNCs. This trend is probably favored by the combination of solvation-induced and electrostatic stabilizations experienced by CNC polar surfaces in water.[42] Other works have suggested that it was hydrogen bonding networks that were responsible for the strong cohesion of CNC agglomerates.[45] Our calculations show that in water, at least, dispersive interactions between the (200) surfaces of CNCs particles are those that require the highest energy to be broken. This is because water molecules can form H-bonds of their own with the hydroxyl groups of CNCs, which minimizes the relative importance of these bonds from a thermodynamic point of view ($\gamma^{w/ps} \approx 6.4$ mN m^{-1}).

The formation of 2-D self-assemblies changes the aspect ratio of the nano-objects that can migrate towards the interface: if they are wide enough, it may become advantageous to orient their polar moieties towards the air/water interface (Fig. 4.e). Indeed, raft-like agglomeration increases the area in polar surfaces that can be exposed at the interface with air (Fig. 4.c&4.e). Hence, while polar surface adsorption still leads to surface energy variations that are smaller than for non-polar surfaces (≈ -26 mJ m^{-2}, instead of ≈ -71 mJ m^{-2}), a raft that is roughly 3 times larger than thicker would preferentially adsorb its polar surfaces at the air/water interface: this could correspond to agglomerates of as little as 2 to 4 nanocrystals depending on their exact cross-section and positioning at the interface. This threshold of aggregation is likely reached in suspension: Uhlig et al.[44] reported 2-D CNC agglomerates that were up to 8 times larger than thicker.

From these calculations, it is possible to propose a speculative mechanism for CNC orientation at the air/water interface: in circumstances where CNCs can migrate to the inter-

face prior to agglomerating, the individual nanocrystals (4.a) orient their non-polar surface towards air (4.f). The film that results from this process is amphiphilic, with stripes of non-polar and polar surfaces (4.i) and f^{nps} reaches its maximum, $f^{\mathrm{nps}}_{\mathrm{max}}$. However, in circumstances where bulk agglomeration is competitive, CNC may first form raft-like assemblies (Fig. 4.b). Upon migration to the interface, these 2-D structures orient their polar surfaces towards the air (Fig. 4.h), which leads to purely polar surfaces upon drying (Fig. 4.h, $f^{\mathrm{nps}} \approx 0$). If it only takes ∼2-4 nanocrystals to form agglomerates that preferentially orient their polar surfaces at the air/water interface, then slight variations in the initial state of CNC aqueous dispersion (caused by the efficiency of the ultrasonication process for instance) can cause fluctuations to the level of amphiphilicity displayed by the films. This is illustrated in Fig. 4.g where the air/water interface is populated by a mix of individual and agglomerated CNCs, which leads to an intermediate content in terms of non-polar surfaces for the film (Fig. 4.k, $0 \leq f^{\mathrm{nps}} \leq f^{\mathrm{nps}}_{\mathrm{max}}$). Note that the representations made in Figs. 4.i-k is coherent with the level of CNC alignment that is observed in AFM analyses (Fig. 1.b).

A process such as spin-coating, in which a significant centrifugal force is applied to the system over a short period of time, likely destabilizes the suspension and favors CNC agglomeration. Spin coating has indeed been reported to favor local concentration increases[46] (which may in turn favor particle/particle agglomeration). It would explain that SC films experimentally display a polar behavior ($f^{\mathrm{nps}} < 0.06$) with a small standard deviation: if the suspension is subjected to a treatment that cause CNC agglomeration, it is possible to repeatably produce a scenario where only agglomerates make it to the interface as in Fig. 4.k. It is worth noting that the shear forces generated by the process may also contribute to orient the 2-D CNC assemblies.

However, a process such as oven-casting is likely to preserve CNC dispersion long enough for individual CNCs to reach the interface, which would explain the amphiphilic behavior displayed by OC films. The impossibilities to completely prevent CNC agglomeration in suspension and to control the ratio between individual and agglomerated CNCs that reach

the interface may be responsible for the large standard deviations observed on OC films: it is harder to repeatably produce and maintain an individual dispersion of CNCs than to repeatably cause their agglomeration. In practice, while it should theoretically be possible to reach $f^{\mathrm{nps}}_{\mathrm{max}}$ (Fig. 4.i), a small fraction of the interface will be made of CNC agglomerates, which lowers f^{nps} (Fig. 4.j). The least polar film we could produce through oven-casting had a f^{nps} of $\sim$0.55 (Fig. 3.a), but there is no way to verify whether this really corresponds to $f^{\mathrm{nps}}_{\mathrm{max}}$ or to the maximum that we could reach given our current protocol.

Based on Fig. 4.i, $f^{\mathrm{nps}}_{\mathrm{max}}$ should be a function of the nanocrystal cross-sectional shape. However, CNC shape cannot be totally resolved through XRD due to the lack of peak for (010) surfaces (see SI) and $\sim$0.55 is currently the best estimate we can provide for our CNCs. Since the CNC dimensions and the cross-sectional shape are a function of their feedstocks,[7,23,24] it should be possible to tune $f^{\mathrm{nps}}_{\mathrm{max}}$ by working with other kind of nanocrystals.

Calculations led here-above may confirm quantitatively whether CNCs find it favorable to orient their (200) surfaces towards the oil at the interface of oil in water Pickering emulsions.[7,18,19] Note that aggregation state was also found to play a role on the interfacial stability of these emulsions.[5,19] Kalashnikova et al.[7],[18] produced CNC stabilized hexadecane in water emulsions. Hexadecane has an interfacial tension of 51.2 $\mathrm{mN\,m^{-1}}$ with water, 22.5 $\mathrm{mN\,m^{-1}}$ with CNC polar surfaces, and 3.0 $\mathrm{mN\,m^{-1}}$ with CNC non-polar surfaces (Table 1). Thus, hexadecane is nearly a perfect match for the (200) surfaces of CNCs: its adsorbtion from the water bulk to the oil/water interface leads to an energy variation of $\sim$-78 $\mathrm{mJ\,m^{-2}}$ (-35 $\mathrm{mJ\,m^{-2}}$ for a polar surface). This provides a quantitative backing to the series of articles by Kalashnikova and co-workers,[7,18,47] which have been cornerstones in the field of CNC stabilized micro-emulsions.

Another interesting result is the comparison between the theoretical energy required to disperse an agglomerate of CNCs in water and the experimental input that needs to be provided to the system in order to do so. A $\sim$7-8 nm wide, $\sim$105-120 nm long nanocrystal has a specific surface area of $\sim$350 $\mathrm{m^2/g_{CNC}}$ (assuming a density of $\sim$1.6 $\mathrm{g/cm^3}$). Since break-

ing CNC-CNC interactions in water requires from ∼13 to ∼59 mJ m^{-2}, dispersing a densely packed agglomerate of CNCs will require ∼5 to ∼20 J/g$_{CNC}$ from a thermodynamic point of view. Experimentally, Beck et al.[45] reported satisfactory dispersion from 950 J/g$_{CNC}$ for spray- and air-dried CNCs at concentrations of 2.8 wt% (∼1.8 vol%). Beuguel et al.[27] mentioned 10 000 J/g$_{CNC}$ as a safer threshold for 1 to 5 wt% (∼0.6-3.1 vol%) CNC suspensions. Hence, the ultrasonication process has an energy efficiency (energy provided to the system over energy required to disperse CNCs) that lies in the range of ∼0.1-1 % for dilute CNC suspensions. This seems plausible since it falls within one order of magnitude of CNC volume fraction (∼0.6-3.1 vol%).

Conclusions

This work proposes the first compelling evidence of CNC orientation at an interface. It provides experimental backing to nearly a decade of research during which this hypothesis has been used to justify the stability brought by CNCs to oil-in-water Pickering emulsions. This was achieved by investigating the influence of the casting protocol on the wettability of CNC thin films. It remained an open-ended question with contact angle variations of up to 30° being reported from sample to sample without convincing explanations. Here, we demonstrate that such variations could be explained by considering the amphiphilicity of the nanocrystals. Liquids are sensitive to molecular-scale heterogeneities and cellulose crystalline surfaces, whose dimensions are nano, are large enough to influence the wetting behaviors.

Based on thermodynamic calculation, a mechanism for CNC orientation at interface is proposed: while individual nanocrystals have an energy incentive to orient their non-polar surfaces to the air interface, CNC agglomerates preferentially expose their polar moieties. This is because CNCs form 2-D assemblies upon agglomeration. Previously reported by Uhlig et al.[44], these raft-like structures find it more stable to orient their largest surfaces, which

happen to be polar, towards air. Hence, in a protocol such as oven-casting during which CNC dispersion is preserved over a long period of time, CNC may migrate as near-individual particles to the interface, which ultimately yields an amphiphilic film. In a spin-coating protocol, however, CNC suspensions are subject to an important centrifugal force that may favor local increases in particle concentration and thus their agglomeration: a polar film is produced. It is worth noting that this mechanism for CNC orientation at interfaces remains to be properly demonstrated: experimentally, this manuscript only demonstrates that while oven-cast films displayed an estimated 0.34-0.50 fraction of non-polar moieties, spin-coated samples stood below 0.06. Reproducibility was lower for the production of amphiphilic films from oven-casting: probably due to its high dependency to the level of initial CNC dispersion. We suggest that working with never-dried CNCs instead of spray-dried particles could improve the repeatability of the process: it would remove the variability introduced during the step of ultrasound-assisted redispersion.

Based on the OWRK model, these calculations on energies and surface composition were made possible via the estimation of CNC surface tension parameters for both the polar and the non-polar surfaces of the nanocrystals: γ^{ps}=53.1±3.0 mN m^{-1} (γ_{D}^{ps}=30.7±2.0 mN m^{-1}, γ_{P}^{ps}=22.4±1.0 mN m^{-1}), and γ^{nps}=31.0±1.6 mN m^{-1} ($\gamma_{\mathrm{D}}^{nps}$=28.0±1.1 mN m^{-1}, $\gamma_{\mathrm{P}}^{nps}$=3.0±0.5 mN m^{-1}). They were obtained by exploiting the empirical correlations that exist between surface tension and Hansen solubility parameters. These coefficients enable for quantitative predictions regarding the behavior of CNC particles at interfaces. Hence, the plausibility of CNC adsorbtion at the oil/water interface could be confirmed: their (200) surfaces are a good match for stabilizing the interface of an hexadecane in water emulsion.[7,18] It was also possible to estimate the energy required to disperse a densely packed agglomerate of CNCs in water: it is in the range of ∼5 to ∼20 J/g$_{\mathrm{CNCs}}$. This provides an element of comparison and an horizon for the redispersion of CNCs:[27,45] the energy optimization of these protocols is crucial to make them industrially relevant.[48] Other applications involve the prediction of CNC behavior in polymer blends and the production of CNC materials with tuned wettability.

Acknowledgements

The authors acknowledge FPInnovations (Pointe-Claire, QC, Canada), PRIMA Québec (grant number FPI NCC RD001), and the National Science and Engineering Research Council (NSERC, grant number RDCPJ 490786-15) for their financial contribution. They are grateful to Celluforce (Montréal, QC, Canada) for kindly providing the cellulose nanocrystals. C. Bruel acknowledge the Fond de Recherche du Québec - Nature et Technologies (FRQNT) for providing him with a scholarship (number 208324). The authors thank Dr. W. Y. Hamad, from FPInnovations, for his contribution in reviewing this work; MM. T. Darlow and T.S. Davies for their contribution to the contact angle measurements; Mr. J.-P. Masse for his help with the XRD analyses; Mrs. P. Moraille for assisting the AFM acquisition; and finally MM. W. Raphael and M. Gauthier for their helpful recommendations and assistance.

Supporting Information description

Supporting Information (SI) provide: a nomenclature for the symbols and abbreviations; a morphological characterization (dimensions, sulfur content, purity, crystallinity) of the CNCs; a list of the precautions that were taken for the wettability model (Eq. 7) to apply; the description of a typical ARCA experiment and the detailed methodology with which the data was analyzed; a film by film breakdown of the ARCA results and their statistical analysis.

References

(1) Tang, J.; Sisler, J.; Grishkewich, N.; Tam, K. C. Functionalization of cellulose nanocrystals for advanced applications. *J. Colloid Interface Sci.* **2017**, *494*, 397–409.

(2) Moreau, C.; Villares, A.; Capron, I.; Cathala, B. Tuning supramolecular interactions of

cellulose nanocrystals to design innovative functional materials. *Ind. Crop. Prod.* **2016**, *93*, 96–107.

(3) Habibi, Y.; Lucia, L. A.; Rojas, O. J. Cellulose Nanocrystals: Chemistry, Self-Assembly, and Applications. *Chem. Rev.* **2010**, *110*, 3479–3500.

(4) Moon, R. J.; Martini, A.; Nairn, J.; Simonsen, J.; Youngblood, J. Cellulose nanomaterials review: structure, properties and nanocomposites. *Chem. Soc. Rev.* **2011**, *40*, 3941–3994.

(5) Capron, I.; Rojas, O.; Bordes, R. Behavior of nanocelluloses at interfaces. *Curr. Opin. Colloid Interface Sci.* **2017**, *29*, 83–95.

(6) Bruel, C.; Tavares, J. R.; Carreau, P. J.; Heuzey, M.-C. The structural amphiphilicity of cellulose nanocrystals characterized from their cohesion parameters. *Carbohydr. Polym.* **2019**, *205*, 184–191.

(7) Kalashnikova, I.; Bizot, H.; Cathala, B.; Capron, I. Modulation of Cellulose Nanocrystals Amphiphilic Properties to Stabilize Oil/Water Interface. *Biomacromolecules* **2012**, *13*, 267–275.

(8) Dankovich, T.; Gray, D. Contact Angle Measurements on Smooth Nanocrystalline Cellulose (I) Thin Films. *J. Adhes. Sci. Technol.* **2011**, *25*, 699–708.

(9) Khoshkava, V.; Kamal, M. R. R. Effect of Surface Energy on Dispersion and Mechanical Properties of Polymer/Nanocrystalline Cellulose Nanocomposites. *Biomacromolecules* **2013**, *14*, 3155–3163.

(10) Javanbakht, T.; Raphael, W.; Tavares, J. Physicochemical properties of cellulose nanocrystals treated by photo-initiated chemical vapour deposition (PICVD). *Can. J. Chem. Eng.* **2016**, *94*, 1135–1139.

(11) Peng, Y.; Gardner, D.; Han, Y.; Cai, Z.; Tshabalala, M. Influence of drying method on the surface energy of cellulose nanofibrils determined by inverse gas chromatography. *J. Colloid Interface Sci.* **2013**, *405*, 85–95.

(12) Yamane, C.; Aoyagi, T.; Ago, M.; Sato, K.; Okajima, K.; Takahashi, T. Two different surface properties of regenerated cellulose due to structural anisotropy. *Polym. J.* **2006**, *38*, 819–826.

(13) Owens, D.; Wendt, R. Estimation of the surface free energy of polymers. *J. Appl. Polym. Sci.* **1969**, *13*, 1741–1747.

(14) Mazeau, K.; Rivet, A. Wetting the (110) and (100) Surfaces of Iβ Cellulose Studied by Molecular Dynamics. *Biomacromolecules* **2008**, *9*, 1352–1354.

(15) Yu, W.; Hou, W. Correlations of surface free energy and solubility parameters for solid substances. *J. Colloid Interface Sci.* **2019**, *544*, 8–13.

(16) Wenzel, R. N. Resistance of Solid Surfaces to Wetting by Water. *Industrial & Engineering Chemistry Research* **1936**, *28*, 988–994.

(17) Reid, M. S.; Villalobos, M.; Cranston, E. D. Cellulose Nanocrystal Interactions Probed by Thin Film Swelling to Predict Dispersibility. *Nanoscale* **2016**, *8*, 12247–12257.

(18) Kalashnikova, I.; Bizot, H.; Bertoncini, P.; Cathala, B.; Capron, I. Cellulosic nanorods of various aspect ratios for oil in water Pickering emulsions. *Soft Matter* **2013**, *9*, 952–959.

(19) Cherhal, F.; Cousin, F.; Capron, I. Structural Description of the Interface of Pickering Emulsions Stabilized by Cellulose Nanocrystals. *Biomacromolecules* **2016**, *17*, 496–502.

(20) Bertsch, P.; Diener, M.; Adamcik, J.; Scheuble, N.; Geue, T.; Mezzenga, R.; Fischer, P. Adsorption and Interfacial Layer Structure of Unmodified Nanocrystalline Cellulose at Air/Water Interfaces. *Langmuir* **2018**, *34*, 15195–15202.

(21) Bertsch, P.; Diener, M.; Adamcik, J.; Scheuble, N.; Geue, T.; Mezzenga, R.; Fischer, P. Corrections to Adsorption and Interfacial Layer Structure of Unmodified Nanocrystalline Cellulose at Air/Water Interfaces. *Langmuir* **2020**, *36*, 1848–1849.

(22) Scherrer, P. Bestimmung der Grőße und der inneren Struktur von Kolloidteilchen mittels Rőntgenstrahlen. *Nachrichten von der Gesellschaft der Wissenschaften zu Gőttingen, Mathematisch-Physikalische Klasse* **1918**, *2*, 98.

(23) Elazzouzi-Hafraoui, S.; Nishiyama, Y.; Putaux, J.-L.; Heux, L.; Dubreuil, F.; Rochas, C. The Shape and Size Distribution of Crystalline Nanoparticles Prepared by Acid Hydrolysis of Native Cellulose. *Biomacromolecules* **2008**, *9*, 57–65.

(24) Sèbe, G.; Ham-Pichavant, F.; Ibarboure, E.; Koffi, A. L. C.; Tingaut, P. Supramolecular Structure Characterization of Cellulose II Nanowhiskers Produced by Acid Hydrolysis of Cellulose I Substrates. *Biomacromolecules* **2012**, *13*, 570–578.

(25) Matthews, J. F.; Skopec, C. E.; Mason, P. E.; Zuccato, P.; Torget, R. W.; Sugiyama, J.; Himmel, H. E.; Brady, J. W. Computer simulation studies of microcrystalline cellulose Iβ. *Carbohyd. Res.* **2006**, *341*, 138–152.

(26) Bruel, C.; Beuguel, Q.; Tavares, J. R.; Carreau, P. J.; Heuzey, M.-C. Apparent structural hydrophobicity of cellulose nanocrystals. *J-FOR* **2018**, *7*, 13–23.

(27) Beuguel, Q.; Tavares, J. R.; Carreau, P. J.; Heuzey, M.-C. Ultrasonication of spray- and freeze-dried cellulose nanocrystals in water. *J. Colloid Interface Sci.* **2018**, *516*, 23–33.

(28) Woodward, R. Contact Angle Measurements Using the Drop Shape Method. 2018; `http://firsttenangstroms.com/pdfdocs/CAPaper.pdf`.

(29) Bruel, C.; Queffelou, S.; Darlow, T.; Virgilio, N.; Tavares, J. R.; Patience, G. S. Experimental Methods in Chemical Engineering: Contact Angles. *Can. J. Chem. Eng.* **2019**, *97*, 832–842.

(30) Good, R. G. Contact angle, wetting, and adhesion: a critical review. *J. Adhes. Sci. Technol.* **1992**, *6*, 1269–1302.

(31) Strobel, M.; Lyons, C. S. An Essay on Contact Angle Measurements. *Plasma Process. Polym.* **2011**, *8*, 8–13.

(32) Good, R. G.; Srivatsa, N. R.; Islam, M.; Huang, H. T. L.; Oss, C. J. V. Theory of the acid-base hydrogen bonding interactions, contact angles, and the hysteresis of wetting: application to coal and graphite surfaces. *J. Adhes. Sci. Technol.* **1990**, *4*, 607–617.

(33) van Oss, C. J.; Good, R. J.; Busscher, R. J. Estimation of the polar surface tension parameters of glycerol and formamide, for use in contanct angle measurements on polar solids. *J. Dispers. Sci. Technol.* **1990**, *11*, 75–81.

(34) Nosonovsky, M. On the Range of Applicability of the Wenzel and Cassie Equations. *Langmuir* **2007**, *23*, 9919–9920.

(35) Hansen, C. M. *Hansen Solubility Parameters A User's Handbook*; CRC Press: Boca Raton, FL, U. S. A., 2007.

(36) Beerbower, A. Surface free energy: a new relationship to bulk energies. *J. Colloid Interface Sci.* **1971**, *36*, 126–132.

(37) Koenhen, D. M.; Smolders, C. A. The determination of solubility parameters of solvents and polymers by means of correlations with other physical quantities. *J. Appl. Polym. Sci.* **1975**, *19*, 1161–1179.

(38) Vavruch, I. On the determination of the factor between cohesive energy density and surface tension. *J. Colloid Interface Sci.* **1978**, *63*, 600–601.

(39) Abbott, S. J.; Hansen, C. M.; Yamamoto, H. Hansen Solubility Parameters in Practice software, eBook, datasets. 2018; url: http://www.hansen-solubility.com, accessed on 2020/01/16.

(40) Jia, L.; Shi, B. A New Equation between Surface Tensions and Solubility Parameters without Molar Volume Parameters Simultaneously Fitting Polymers and Solvents. *J. Macromol. Sci. B* **2011**, *50*, 1042–1046.

(41) de Meijer, M.; Haemers, S.; Cobben, W.; Militz, H. Surface Energy Determinations of Wood: Comparison of Methods and Wood Species. *Langmuir* **2000**, *16*, 9352–9359.

(42) Bruel, C.; Davies, T. S.; Tavares, J. R.; Carreau, P. J.; Heuzey, M.-C. Self-assembly behaviors of colloidal cellulose nanocrystals: A tale of stabilization mechanisms. *J. Colloid Interface Sci.* **2020**, *574*, 399–409.

(43) Mundo, R. D.; Palumbo, F. Comments Regarding An Essay on Contact Angle Measurements. *Plasma Processes and Polymers* **2011**, *8*, 14–18.

(44) Uhlig, M.; Fall, A.; Wellert, S.; Lehmann, M.; Prévost, S.; Wågberg, L.; von Klitzing, R.; Nyström, G. Two-dimensional aggregationand semidilute ordering in cellulose nanocrystals. *Langmuir* **2016**, *32*, 442–450.

(45) Beck, S.; Bouchard, J.; Berry, R. Dispersibility in Water of Dried Nanocrystalline Cellulose. *Biomacromolecules* **2012**, *13*, 1486–1494.

(46) Zhao, Y.; Marshall, J. S. Spin coating of a colloidal suspension. *Phys. Fluids* **2008**, *20*, 043302.

(47) Kalashnikova, I.; Bizot, H.; Cathala, B.; Capron, I. New Pickering emulsions stabilized by bacterial cellulose nanocrystals. *Langmuir* **2011**, *27*, 7471–7479.

(48) Nelson, K.; Turpin, D. Advancing Commercialization of Nanocellulose: Critical Challenges Workshop Report. 2020; https://doi.org/10.13140/RG.2.2.33789.59363.

Graphical TOC Entry

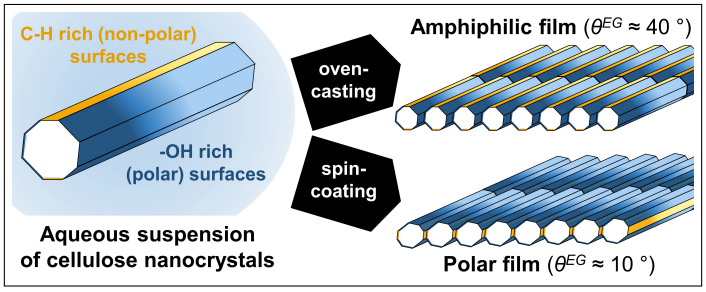

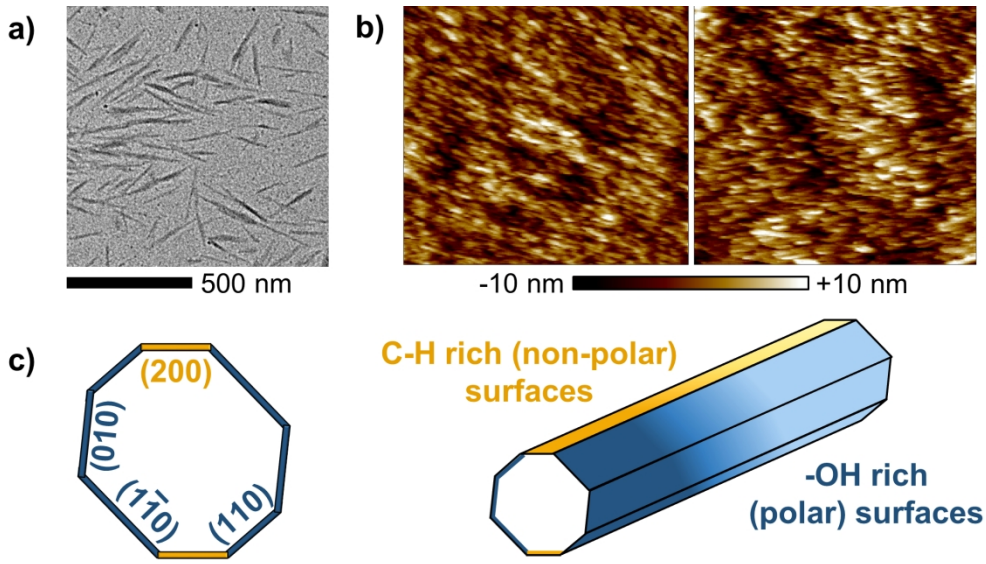

Morphology and representation of cellulose I_β nanocrystals. **(a)** TEM image of individual and agglomerated CNCs. **(b)** AFM height images of spin-coated (left) and oven-cast (right) CNCs. Micrographs are 2 μm wide and were flattened (by a second-order polynomial) in order to remove their mesoscale roughness. **(c)** On the left is the cross-section of a cellulose I_β: polar surfaces –(010), (110), and (1-10) lattice planes– are plotted in blue, and non-polar ones –(200) lattice planes– are in yellow. On the right is a scheme of the octogonally-shape nanocrystal: its lateral surfaces are constituted of polar and non-polar stripes.

90x49mm (600 x 600 DPI)

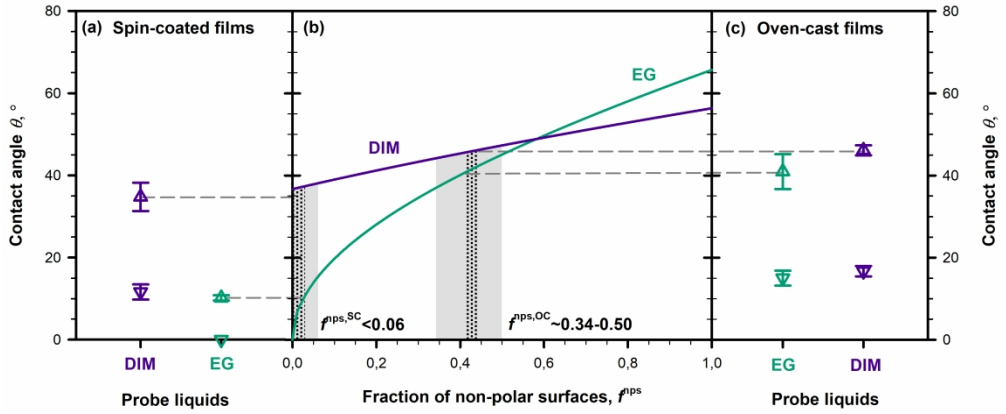

ARCA results for spin-coated **(a)** and oven-cast **(c)** films and their predictions in terms of non-polar fraction, f^{nps}, for the air/sample interface **(b)**. EG and DIM results are plotted in green and purple, respectively. Average θ_a values are represented by empty triangles up and θ_r values by empty triangles down. In **(b)**, filled lines are the plots of θ_a as a function of f^{nps} (Eq. 7) for EG and DIM. The projection of θ_a values (grey dashed lines) over these plots provides estimates for the samples' surface content in non polar surfaces. The consistency observed between the f^{nps} predictions derived from EG and DIM (with ~0.02-0.03 between both predictions, highlighted by the dotted areas) confirms the validity of CNC surface tension parameters. Error bars in **(a)**&**(c)** are standard deviations. Their influence on the determination of f^{nps} is highlighted by the grey areas in**(b)**.

166x80mm (600 x 600 DPI)

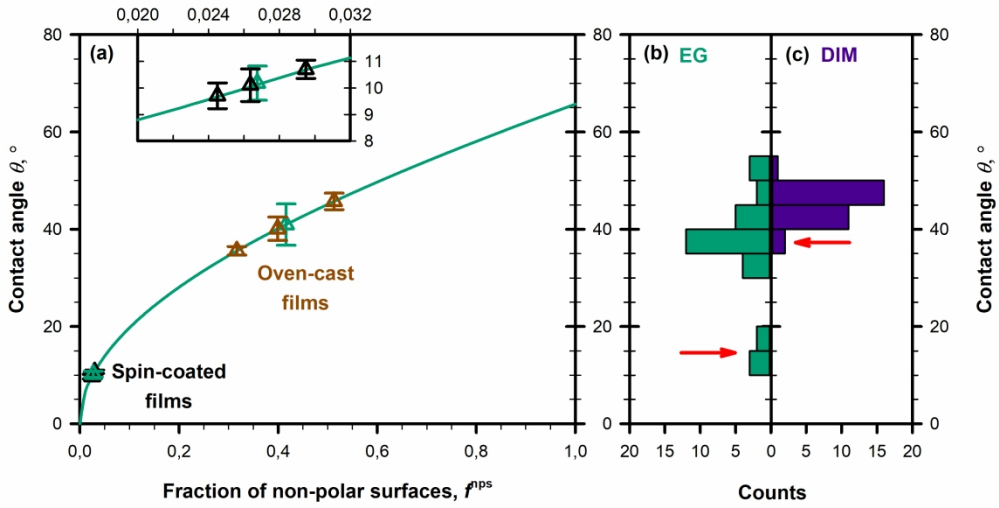

Repeatably of CNC orientation during the spin-coating and oven-casting processes based on EG results **(a)**. The green line and the green triangles up are the plots for Eq. 7 and for the average advancing CA values (see Fig. 2). The black and brown triangles up represent the advancing CA values measured for each of the spin-coated and oven-cast films, respectively. The insert is a zoom of the spin-coated results for greater readability. Error bars are standard deviations. Sessile drop measurements taken on 7 additional oven-cast films with EG **(b)** and DIM**(c)**. The results pointed by the red arrows are from a single data set, taken on a film that apparently failed to orient its non-polar functionalities at the air/sample interface to the same extent as the 6 other samples.

141x80mm (600 x 600 DPI)

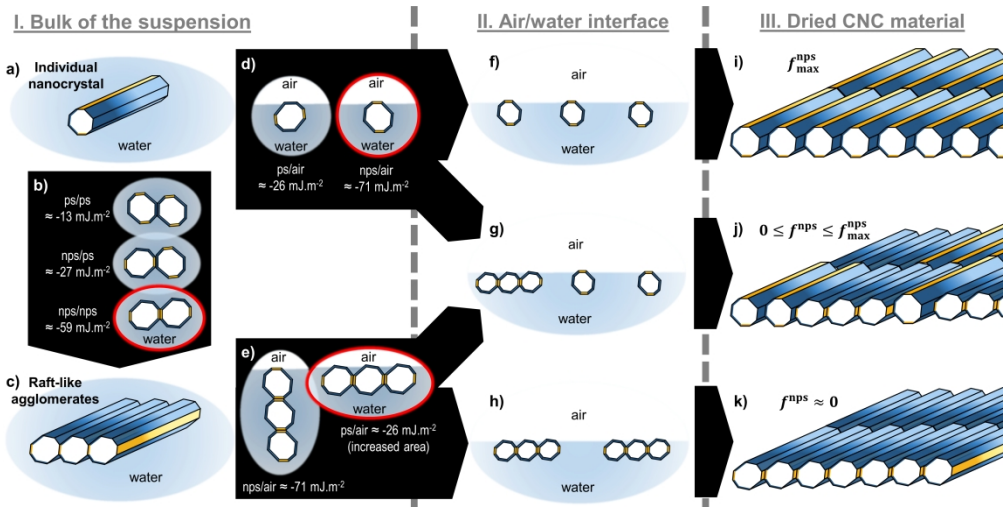

Speculative mechanism for CNC orientation at the air/sample interface. Assuming CNCs are initially well dispersed **(a)**, they may either migrate to the air/water interface as individual nanocrystals or first agglomerate in the water bulk. Upon agglomeration **(b)**, CNCs preferentially assemble their non-polar surfaces to form raft-like structures **(c)**. Upon migration towards the air/water interface, individual CNCs orient their non-polar surfaces towards the air **(d)**. 2-D agglomerates may, however, prefer to orient their polar surfaces if their cross-sectional aspect ratio is large enough **(e)**. Depending on the state of CNC dispersion within the water bulk, the air/water interface may be populated by individual nanocrystals only **(f)**, by a mix of individual and agglomerated particles **(g)**, or by agglomerated CNCs only **(h)**. Upon casting, these result into thin films whose surface is either amphiphilic **(i)**&**(j)** or purely polar **(k)**. The fraction of non-polar surfaces that a film can expose should reach a maximum of f^{nps}_{max} in **(i)**, whose amplitude is a function of the nanocrystals' geometry, and a minimum of ~0 in **(j)**.

180x90mm (600 x 600 DPI)